Cement and Concrete Research 42 (2012) 215–221

Contents lists available at SciVerse ScienceDirect

Cement and Concrete Research

journal homepage: http://ees.elsevier.com/CEMCON/default.asp

Short communication

On the use of peak-force tapping atomic force microscopy for quantification of the local elastic modulus in hardened cement paste

Pavel Trtik [a,*], Josef Kaufmann [a], Udo Volz [b]

[a] Empa, Swiss Federal Laboratories for Materials Science and Technology, Dübendorf, Switzerland
[b] Bruker Nano GmbH, Mannheim, Germany

ARTICLE INFO

Article history:
Received 31 March 2011
Accepted 17 August 2011

Keywords:
Microstructure (B)
Atomic force microscopy (B)
Image analysis (B)
Elastic moduli (C)

ABSTRACT

A surface of epoxy-impregnated hardened cement paste was investigated using a novel atomic force microscopy (AFM) imaging mode that allows for the quantitative mapping of the local elastic modulus. The analyzed surface was previously prepared using focussed ion beam milling. The same surface was also characterized by electron microscopy and energy-dispersive X-ray spectroscopy.

We demonstrate the capability of this quantitative nanomechanical mapping to provide information on the local distribution of the elastic modulus (from about 1 to about 100 GPa) with a spatial resolution in the range of decananometers, that corresponds to that of low-keV back-scattered electron imaging. Despite some surface roughness which affects the measured nanomechanical properties it is shown that topography, adhesion and Young's modulus can be clearly distinguished.

The quantitative mapping of the local elastic modulus is able to discriminate between phases in the cement paste microstructure that cannot be distinguished from the corresponding back-scattered electron images.

1. Introduction

Within the last two decades, a number of publications on assessment of the nanomechanical properties of cement based materials have been published. The objective of this nanomechanical testing is to assess the mechanical properties of the individual constituents of heterogeneous materials and in this way provide a meaningful experimental input for a (multiscale) modeling. Nanoindentation has been a widely used technique hitherto utilized for the purpose. It was recently shown that statistical nanoindentation might not be the optimum testing technique for the elucidation of mechanical properties of microstructured porous multiphase materials. In particular, the issues of the surface roughness due to the intrinsic porosity of cementitious materials [1], the partial volume effects within the nanoindentation interaction volumes [2,3] and the statistical evaluation of the elastic modulus histograms [4] were shown to pose serious obstacles for the provision of reproducible and unambiguous results.

Despite all the above-mentioned problems, the statistical nanoindentation remains a popular technique for assessment of mechanical properties on micro- and nanoscale [e.g. [5–9]. In the search of a different technique for the purpose that would circumvent at least some of the problems inherent to the statistical nanoindentation, we identified peak-force tapping atomic force microscopy (further only 'peak-force tapping AFM') as one of the possible alternatives. This technique so far was applied to quantify the elastic properties of materials in a lower GPa (0–10 GPa) range [10]. Here we present the results of a pilot test that was performed on a sample of epoxy-impregnated hardened cement paste and show that this range can be extended to higher values of elastic modulus (<~100 GPa).

2. Peak-force tapping atomic force microscopy

Atomic force microscopes can be also utilized for (statistical) nanoindentation testing. Even though AFM-based nanoindenters have a minor advantage over the standard nanoindentation instruments in the ability of imaging the sample surface before the actual indentation is performed, the nanomechanical properties are derived according to the same principles [11] and therefore AFM-nanoindentation [12] does not significantly differ from the above-mentioned statistical technique.

Interestingly, atomic force microscopy (AFM) has been long recognized as a useful instrument for the assessment of the local mechanical properties of materials. The force volume AFM mode, a collection of the force–separation curves at each pixel, allows for the mapping of the elastic properties [13]. Unfortunately, the large amount of information that needs to be processed limits this kind of elastic properties mapping to very low imaging speeds and low resolution. On the other hand the tapping AFM mode can provide phase contrast maps that allow for a qualitative distinction of materials with different mechanical and/or interaction properties. Here, the extraction of quantitative mechanical properties is not possible because the adhesion forces cannot be unambiguously separated from the elastic behavior.

* Corresponding author. Tel.: +41 44 823 42 99.
E-mail address: pavel.trtik@empa.ch (P. Trtik).

0008-8846/$ – see front matter © 2011 Elsevier Ltd. All rights reserved.
doi:10.1016/j.cemconres.2011.08.009

Recently, Sahin and Erina [14] showed that a novel variant of tapping-mode AFM utilizing when special torsional force-sensing probes (Harmonix™) can be conveniently used for the mapping of elastic modulus and adhesion forces. With a working range of elastic moduli from a few MPa to a few GPa this mode is limited to soft materials e.g. polymers.

Peak-force tapping AFM is a new operating mode of AFM that can operate with a wide variety of standard AFM probes. In peak-force tapping AFM the probe is oscillated at a typical frequency of 2 kHz (far below the resonance of the cantilever) with typical peak-to-peak amplitudes in air of 300 nm. This brings the probe periodically into contact with the sample for a short period of time [<100 μs] and a periodically oscillating force is exerted onto the sample surface. Thanks to the high speed of modern AFM controllers, the individual force versus separation curves can be collected for each tap of the probe onto the sample. The schematic diagram of the collected force–separation curve is shown in Fig. 1.

The novelty of the presented peak-force tapping AFM technique lies in the control of the maximum normal force (the 'peak force') that is applied on the sample at each point of the AFM map (in tapping mode AFM only the damping of the cantilever oscillation is controlled which is not directly related to the applied tip–sample forces). Thanks to the feedback system, this maximum force is kept constant throughout the scan. The information about sample adhesion, surface deformation and topography can be unambiguously separated from the individual force–separation curves at each position of the scan. Interestingly, the force–separation curves are in principle comparable to the load–displacement curves utilized for evaluation of modulus in nanoindentation. In order to elucidate the elastic properties from peak-force tapping AFM, the Derjaguin–Muller–Toporov (DMT) model [16] can be used for the estimation of the sample's reduced elastic modulus. According to this model the forces during the tip–surface interaction are described by Eq. 1:

$$F_{\text{interaction}} = \frac{4}{3}E^{*}\sqrt{R(d-d_0)^3} + F_{\text{adh}} \tag{1}$$

where $F_{\text{interaction}}$ is the tip–sample force, E^* is the reduced elastic modulus of the tip and the sample, R is the tip radius, d_0 is the surface rest position, $(d-d_0)$ is the sample deformation, and F_{adh} is the adhesion force during the contact. The Young's modulus of the sample E_s can be derived as from the following equation:

$$E^{*} = \left[\frac{1-\nu_s^2}{E_s} + \frac{1-\nu_{tip}^2}{E_{tip}}\right]^{-1} \tag{2}$$

where ν_s is the Poisson's ratio of the sample, ν_{tip} is the Poisson's ratio of the probe, E_s is the Young's modulus of the sample and E_{tip} is the Young's modulus of the probe. For the experiments reported here, the value of Poisson's ratio of the sample was assumed to be 0.3. In the range from 0.2 to 0.4 which are typical values for Poisson ratio of mineral phases, the error as estimated from Eq. 2 is less than 10%. A diamond probe with a high stiffness was used to minimize the influence of the probe. The influence of the probe stiffness in this pilot test was neglected. For the here reported maximal elastic modulus value of 133 GPa this leads to a maximal error of about 12%.

Several calibrations must be performed in order to receive quantitatively reliable outcomes.

First, the tip rounding calibration was performed by the tip producer using a 'tip evaluation' sample made of polycrystalline titanium coating. The radius of curvature was thus estimated to be equal to 50 nm. Second, the cantilever spring constant was calibrated by the instrument producer. The calibration spring constant provided by this calibration was equal to 212 Nm^{-1}. Third, in a cantilever-based force–displacement measurements, the measured cantilever's deflection D contains the information about the applied force F and about the sample deformation $(d-d_0)$ as well. In order to separate these two pieces of information, the response of the cantilever on an infinitely stiff surface (i.e. so-called deflection sensitivity, S in [m/V]) has to be determined. Sapphire sample served as an approximation to the infinitely stiff sample on which the deflection sensitivity was calibrated.

Once the deflection sensitivity is known, the applied force F and the tip position d can be calculated as follows:

$$F = k \cdot S \cdot D \tag{3}$$

$$d = z - S \cdot D \tag{4}$$

where D denotes the cantilever deflection (measured in Volts), z is the vertical scanner position and k is the cantilever spring constant.

As the additional part of the calibration routine, the sample of highly-ordered ordered pyrolitic graphite (HOPG-15 M, expected elastic modulus of 18 GPa as stated by the producer) was investigated. The area of 256×256 points over 5×5 μm scanned resulting in the average value of modulus 21 GPa ± 3.2 GPa. Parts of the image however exhibited relatively high adhesion values thus suggesting local tip and/or sample contamination. On a smaller subset of this scan that exhibited the usual values of adhesion (64×64, 1.25×1.25 μm) the average value has been equal to 19.5 ± 2.0 GPa. Even though the average values deviate slightly from the expected value of 18 GPa, the results remain within one-standard-deviation range from the expected value.

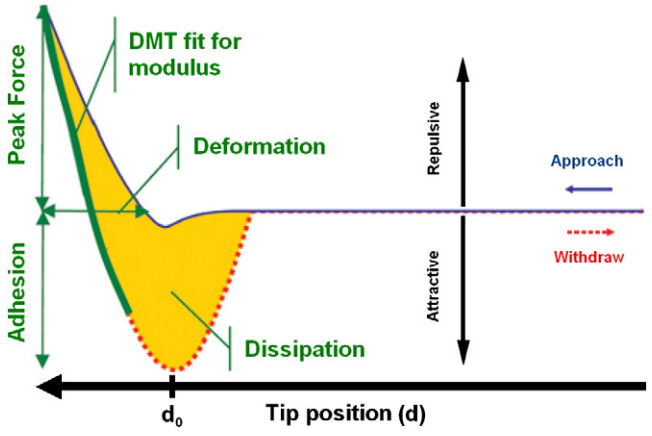

Fig. 1. Schematic diagram of a force vs. separation curve for the single cycle of the peak-force tapping AFM (blue — tip approach, red — tip withdrawal). In the peak-force tapping AFM the maximum force ('peak force') is set to be constant for each measurement position. The peak force used in this investigation equaled 3 μN. The sample deformation was in the range between 3 and 12 nm. The entire tip–sample separation cycle was about 600 nm. The image is adapted from Ref. [15].

3. Materials and methods

The 20×20×10 mm block of hardened cement paste (w/c = 0.5) was produced from white Portland cement (Aalborg white) and water cured for 21 days. After that, the block was impregnated using common methods for epoxy-impregnation. After the epoxy impregnation, a small cylindrical sample originally residing inside the block was prepared by high-current FIB milling and fixed at the end of a stainless steel sample holder (see Fig. 2).

The cylindrical sample was fixed on the stainless steel holder. The surface on the top face of the cylinder was then smoothed using low-current FIB milling and served as the surface for the nanomechanical

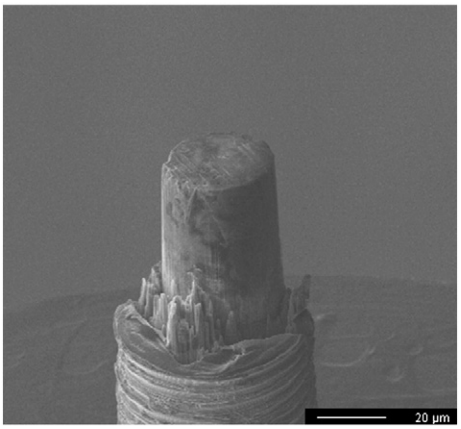

Fig. 2. The sample epoxy impregnated hardened cement paste. The top surface of the sample was investigated using peak-force tapping AFM.

mapping. A low-keV (1.2 keV accelerating voltage) back-scattered electron image of the surface was then acquired using an energy selective detector (EsB). We would like to highlight here that the focus of the sample preparation was to prepare an as flat as possible surface that would be – at the same time – easily accessible to peak-force tapping AFM probe. In principle, the sample preparation might be much simplified (utilization of the standard grinding and polishing of epoxy-impregnated specimen).

Nanomechanical mapping was performed at Bruker Nano GmbH (Mannheim, Germany) using a Dimension Icon instrument in PeakForce tapping mode with quantitative nanomechanical analysis (QNM). The instrument was equipped with a three-face 90-degree corner cube diamond probe on a steel cantilever (stiffness approximately 212 Nm^{-1}, and of the radius of the tip rounding about 50 nm). The peak-force set-point was adjusted to 3.0 μN and the Poisson's ratio was assumed to be equal to 0.3 for the entire 512×512 pixels (20×20 μm) scan of the sample. The line scan rate was equal to 0.5 Hz. After the nanomechanical mapping the surface was analyzed using energy dispersive X-ray spectroscopy (EDX) and electron microscopy (using a standard solid-state back-scattered electron detector) at 10 keV.

4. Results and discussion

Fig. 3 shows the 512×512 maps of the topography, adhesion, sample deformation and Young's modulus of a square region of the top plane of the sample as acquired by peak-force tapping AFM.

Even though the sample preparation should result in a very low surface roughness of the investigated surface, the root-mean-square surface roughness based on the topography map (see Fig. 3a) equaled 38.5 nm. Apart from the general waviness of the surface, waterfall artifacts of FIB milling are observed. The waterfall artifacts are the parallel, from the vertical about 15-degrees tilted, dark lines (i.e. surface depressions) in the topography image with a depth in the order of several tens of nanometers. The RMS of the entire 512×512 image is actually strongly influenced by the presence of the FIB waterfall artifacts that lead to a relatively high value of RMS surface roughness for the entire (512×512) image. When the RMS surface roughness is analyzed locally for all the measuring positions on areas of about

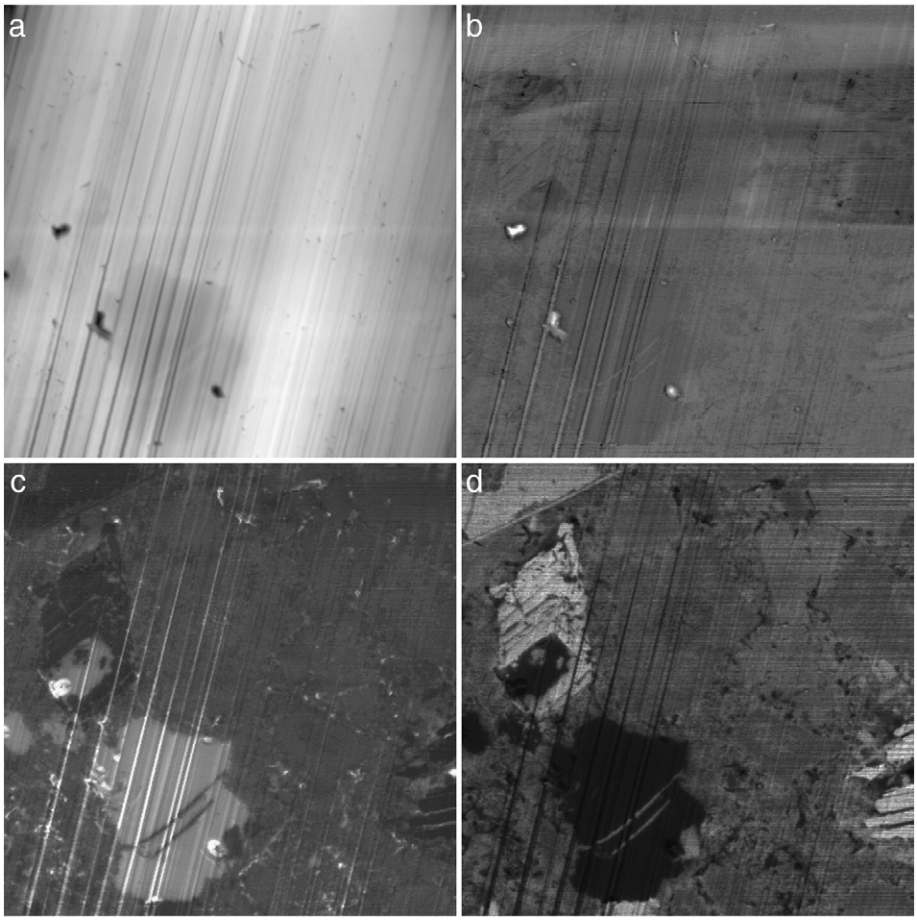

Fig. 3. The results of the peak-force tapping atomic force microscopy: (a) topography — black corresponds to −250 nm, white corresponds to + 100 nm; (b) adhesion force 0–1 μN, (c) sample deformation 0–20 nm, (d) Young's modulus 0–100 GPa. The gray level in each image varies between black and white color limits that are mentioned above for each of the presented property. The size of the 512×512 pixel maps was set to be 20 μm.

156 nm × 156 nm in size, the local RMS roughnesses vary widely between 0.2 and 59.6 nm. However, the respective mean and median values of all these local RMS roughnesses are 5.3 nm and 3.3 nm only. These values indicate that the surface between the individual waterfall artifacts are actually of rather low surface roughness that seems to be sufficiently low for successful peak-force AFM testing.

Significantly lower elastic modulus but higher adhesion is measured in the areas of the surface defects. This observation underlines the importance of low surface roughness for the nanomechanical testing of multiphase materials and poses some constraint on the use of peak-force tapping AFM on the unimpregnated hardened cement pastes, for which much higher values of surface roughness (due to the intrinsic sample porosity) must be expected (see Ref. [1]).

Fig. 4 presents histograms of adhesion, surface deformation and elastic moduli of the corresponding maps shown in Fig. 3. The tip adhesion force was contained below 500 nN for the vast majority of the measurement points, which suggests that the tested surface was clean and uncontaminated. The measured surface deformations induced by the oscillating normal force were mostly contained between 3 nm and about 12 nm (which is clearly below the tip radius of ~50 nm).

The sample deformation and the adhesion maps – as derived from the force vs. separation curves – exhibit some contrast of the microstructural features. This 'microstructural contrast' can be observed clearly in the map of the elastic modulus that is derived from the values of the sample deformation and adhesion by Eqs. 1 and 2. All the measured values of the elastic modulus were in the range from 0.7 to 133 GPa. However, only 0.1% of the values were higher than 84 GPa. Further, we attempt to follow the logic of investigations of Hughes and Trtik [17] and Chen et al. [18] in correlating the information stemming from the nanomechanical testing with the scanning electron microscopy (SEM) and/or energy dispersive X-ray spectroscopy (EDX). The elastic modulus map was 2D affinely registered [19] with both electron microscopy images. The 1.2 keV backscattered electron image is shown in Fig. 5a, while the 10-keV backscattered electron image is shown in Fig. 5b. The same image with the 2D affinely registered elastic modulus map is shown in Fig. 5c. The affinely registered map of elastic modulus is rotated about 15° anticlockwise and scaled down by a factor ranging from 0.95 to 0.97 (depending on the image direction).

Clear microstructural features can be discerned in all three images presented in Fig. 5. In all images, the porosity appears dark with the largest area of porosity occurring just below the center of the investigated circular surface area. This large spot of porosity is crossed from the bottom-left to the top-right by apparent cross-section of two parallel platelets of approximately 200 nm in thickness. Two residues of unhydrated particles (exhibiting the brightest 10-keV electron microscopy contrast) can be observed. The unhydrated particles show striations similar to some observed by Scrivener [20], thus suggesting the unhydrated residues are composed of belite. The apparent thickness of some of the striations in the sub-100-nm domain can be observed both in the SEM images and in the elastic modulus maps. Areas that can be apparently identified as calcium hydroxide (light gray) and C–S–H (dark gray) can be observed in 10-keV electron microscope image.

In order to analyze the phase composition in more detail an EDX mapping was performed (see Fig. 6). The information stemming from the two types of electron microscopies and from EDX mapping were used for provision of the image masks of four phases, namely, epoxy-impregnated pore space, partially hydrated clinker residues, calcium hydroxide and other hydrates (see Fig. 7b). Based on the composition of the used cement and from the EDX data the fourth phase should be predominantly composed of calcium silicate hydrates (C–S–H). Although there is a clear contrast in the elastic modulus mapping (Fig. 3d) in the regions containing this hydrate phases, the selected resolution in this pilot test (512 × 512 pixels of a 20 μm region) is too low to clearly distinguish different C–S–H phases (e.g. low/high density C–S–H) or other hydration products. In this paper we hence focus on the clearly distinguishable phases and treat this region consequently in a more general way. However, principally much higher resolutions similar to the ones for standard tapping AFM-images are possible (increasing the number of pixels, limitation to smaller areas of interest), which then would permit a more detailed analysis of the different hydrate phases.

For the interaction volume of the 1.2 keV electrons detected by EsB detector that is significantly lower than the one of the 10 keV electrons detected by solid-state detector, the 1.2-keV electron image of the FIB-milled sample surface allows for very high-resolution segmentation of the epoxy-impregnated pore space and solid phases. On the other hand, the contrast of solid phases is suppressed in the EsB-based image [21] and becomes apparent only in the higher (10 keV) electron image. Consequently, the 1.2-keV image was used for provision of the mask of the epoxy-impregnated pore-space by simple global thresholding. The simple thresholding of 10-keV image applied locally to the manually selected regions that included the partially hydrated clinker residues was used for the provision of the mask of this phase. The simple thresholding cannot be used for separation of calcium hydroxide domains from the other solids in the 10-keV electron microscopy image. Therefore, the information based on the combination of 10-keV electron microscopy and EDX mapping was used for manual identification of mask of CH. The areas of the surface not covered by either of the above-mentioned masks were considered belonging to the phase of other hydrates. The elastic moduli of the identified phases (shown in Fig. 7b) are summarized in Table 1.

The elastic modulus of the phase identified as the epoxy-impregnated pore space (Fig. 7b, black) is about 8.4 ± 4.5 GPa. This compares well with the value reported by Sorrelli et al. [22] for the

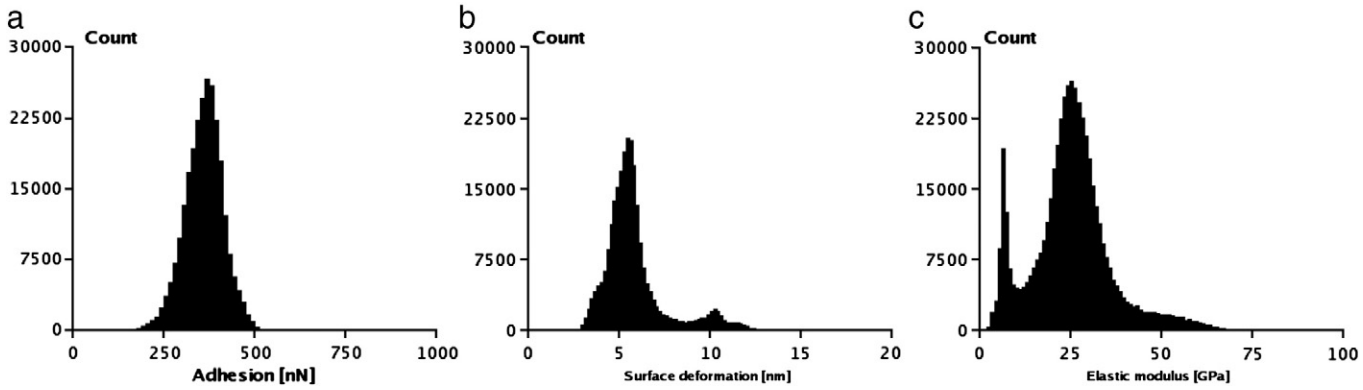

Fig. 4. Image histograms of (a) adhesion, (b) surface deformation, and (c) elastic modulus. The histograms are based on 512 × 512 (i.e. on 262,144) measurement points.

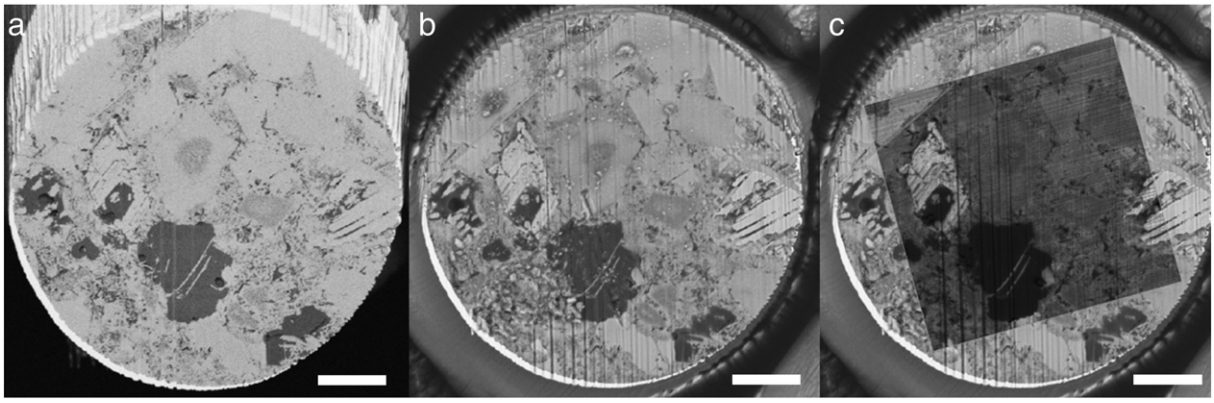

Fig. 5. Correlation electron microscopy with the elastic modulus map of peak-force tapping AFM: (a) 1.2 keV EsB back-scattered electron image, (b) 10 keV back-scattered electron image, (c) 10 keV back-scattered electron image with the 2D affinely registered elastic modulus map. The scale bars correspond to 5 μm.

elastic modulus of the epoxy-unimpregnated micro-porosity using statistical nanoindentation (7.0 ± 4.0 GPa).

The elastic modulus of the phase identified as the partially hydrated clinker residues (Fig. 7b, white) is 58.7 ± 11.4 GPa. This value is very much lower than the values of elastic modulus that was found out experimentally for the pure unhydrated phases by Velez et al. [23]. Interestingly, the results of coupled nanoindentation and SEM/EDX investigation by Chen et al. show that the elastic modulus of unhydrated cement particles in cement pastes ranges from about 30 to 160 GPa [18]. This relatively large variation can be possibly explained (among other reasons) by the occurrence of the calcium-leached zone in the clinker residues. Based on the nuclear resonant reaction analysis (NRRA) of C_3S particles, the calcium-leached zone is reported to be as much as 1.5 μm thick [24]. We note that the surface investigated here sectioned only two areas of clinker residues and the observed striations actually assured that there is no part of the clinker residue mask that would be further away from the hydrated boundary than 1 μm. In other words, the relatively low value of the average elastic modulus could be possibly explained by the occurrence of the calcium-leached zones. Further research is required on this issue and the peak-force AFM is envisaged to provide a tool (complementary to NRRA) for the assessment of the extent of the reaction zones during the cement hydration.

The elastic modulus of the phase identified as other hydrates (Fig. 7b, dark gray) was found to be 25.5 ± 8.6 GPa. Even though this phase is predominantly composed of C–S–H, other hydration products surely occur within this phase. The histogram of the elastic moduli of this phase is shown in Fig. 8. The histogram does not seem to provide any clear indication for the occurrence of more than one type of C–S–H. However, it needs to be highlighted here

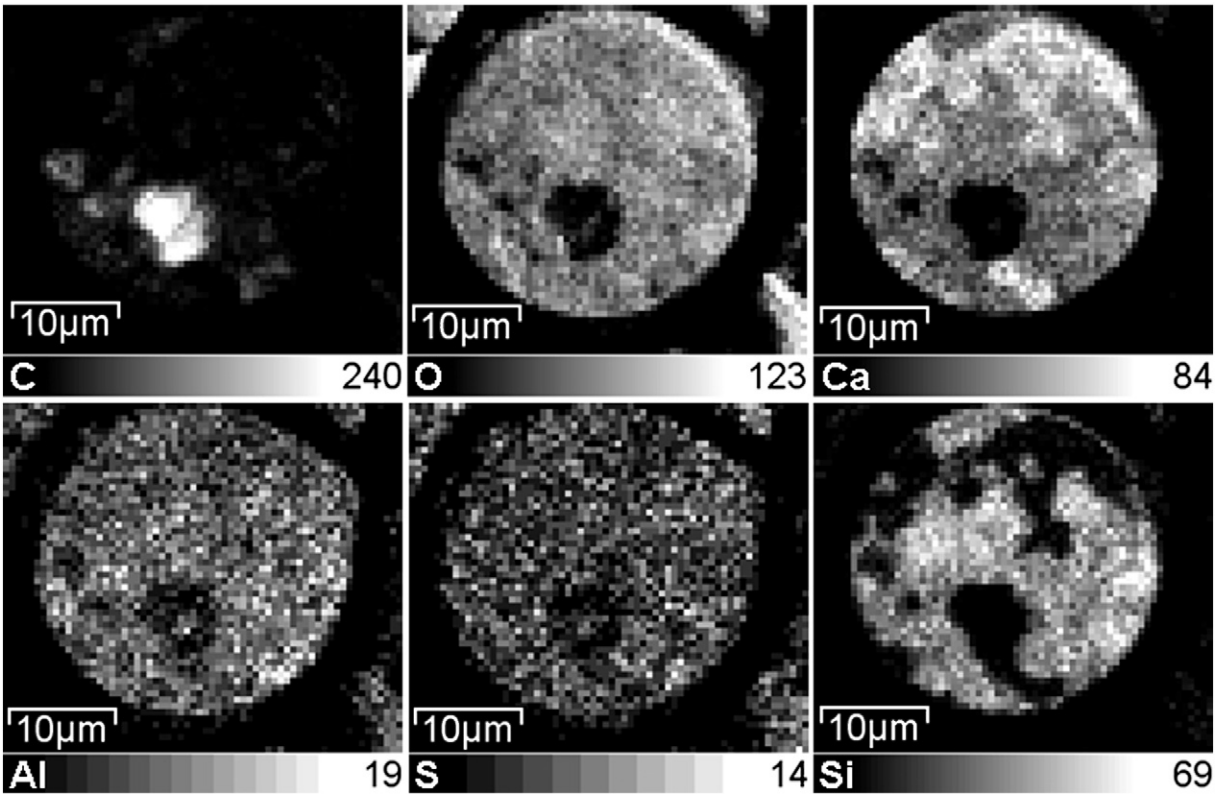

Fig. 6. Energy dispersive X-ray EDX elemental maps of carbon, oxygen, calcium, aluminum, sulfur and silicon performed at 10 keV. The grayscales are shown separately for each particular elemental map.

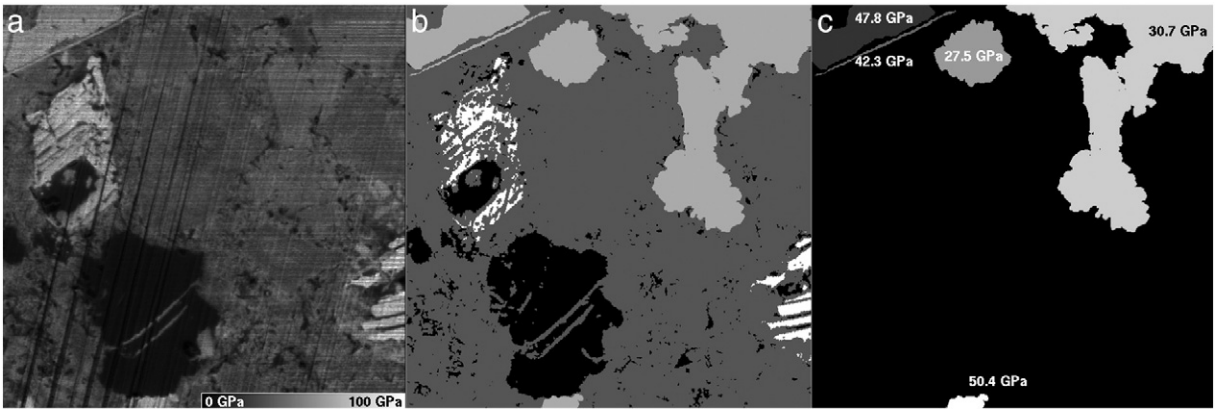

Fig. 7. Segmentation of phases based on the congruent datasets: (a) elastic modulus map; (b) segmentation to porosity (black), unhydrated residues (white), calcium hydroxide (light gray) and other hydrates (dark gray); (c) the mask of five independent regions of calcium hydroxide. The average values of the elastic modulus of each region are given in the image.

that the size of the investigated area (20 μm × 20 μm) is not representative and therefore no strong conclusions about the number of C–S–H types should be based on this result.

The average elastic modulus of the phase identified as portlandite (Fig. 7b, light gray) equals 33.5 ± 9.1 GPa. However, clearly separated regions of portlandite exhibiting distinctly different elastic moduli can be found in the elastic modulus map. In a further analysis and in order to show some striking differences between electron microscopy images and and elastic modulus mapping, the CH containing phases were analyzed in more detail. The mask of five clearly separable areas as derived from the elastic modulus mapping (identified as calcium hydroxide in the segmentation map 7b) is shown in Fig. 7c. The average elastic modulus in each of these calcium hydroxide regions assumes quite different values between 27.5 and 50.4 GPa.

It has been reported that the elastic properties of calcium hydroxide strongly depend on the crystal orientation [25]. Laugesen [26] derived that the Young's modulus may vary between 26 and 99 GPa depending on the angle between the crystal c-axis and the direction of deformation. As shown in Fig. 7c, the peak-force AFM seemingly revealed differently oriented domains of calcium hydroxide. We suggest that this observation highlights the drawbacks of the evaluation of the nanomechanical test results by fitting the normal distribution functions into the elastic modulus histograms. For the statistically representative dataset of nanomechanical tests performed on the representative sample area, the distribution of Young's modulus of calcium hydroxide will not be normal. The normal distribution of portlandite may appear only in the case of statistically non-representative datasets of nanomechanical tests. For these reasons and despite the very high number of measurement points (262,144), we therefore refrain from performing an exercise of fitting multiple normal distribution functions into the peak-force tapping AFM elastic modulus histogram (like Fig. 4c).

Regarding the quantitative value of the presented results, we must state that the average values of elastic moduli of the identified phases surely depend on (i) how many phases can be reasonably identified in the microstructure and (ii) on the way the identified phases are segmented. We stress that the way the segmented map of the material phases (see Fig. 7b) was created is only one of very large number of possible ways of the material phase segmentation.

Also, the image distortions (due to drift/charging in SEM, drift/zero-point identification' for the peak-force tapping AFM) can significantly influence the image registration. In the case of occurrence of large distortions, non-affine registrations of SEM and peak-force tapping AFM images might need to be applied. In the case presented here, the affine registration of the entire images was sufficient and we show the capability of the peak-force tapping AFM to quantitatively distinguish regions of different elastic moduli with spatial resolution of about 100 nm in size. (e.g. the portlandite platelet in the top left corner of the elastic modulus map). In this sense, the peak-force tapping AFM provides a promising imaging tool with the spatial resolution similar (or superior to) that of low-keV scanning electron microscopy. Consequently, the information stemming from these independent testing techniques can be easily correlated.

The advantages of the peak-force tapping AFM over statistical nanoindentation are as follows:

(i) The peak-force tapping AFM exerted surface deformations in a several nanometer domain (see Fig. 4b). As a result, peak-force tapping AFM has a much smaller interaction volume than usually applied in the statistical nanoindentation (about 1 μm^3). Therefore, the probability that pure phases are investigated by peak-force tapping AFM is higher than in the case of nanoindentation. In other words, the nanomechanical test results are less affected by the microstructurally intrinsic partial volume effects.

(ii) The peak-force tapping AFM can provide very large number of independent nanomechanical measurements in a rather short time. The statistical nanoindentation datasets that are found

Table 1
The average peak-force AFM elastic moduli of the identified material phases.

Materials phase	Elastic modulus [GPa]
Epoxy-impregnated pore space	8.4 ± 4.5
Other hydrates	25.5 ± 8.6
Calcium hydroxide	33.5 ± 9.1
Partially hydrated clinker residues	58.7 ± 11.4

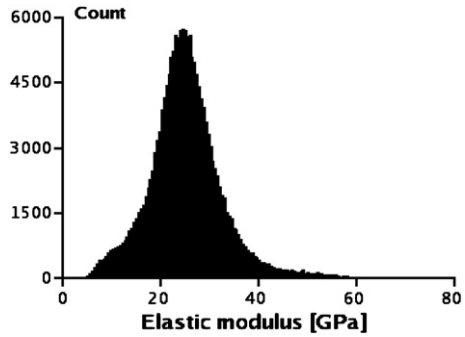

Fig. 8. Histogram of the peak-force elastic moduli of phase identified as other hydrates. The phase is predominantly composed of C–S–H.

in the literature usually consists of few hundreds of the individual tests. The presented scan consists of 262,144 data points that were acquired within 17 min.

Regarding the future experiments that may yield information from the representative sample areas, we note that in the utilized test arrangement, scans as large as approximately 90×90 μm are possible with size up to 5000×5000 pixels. However, it needs to be highlighted that scans of such size may take very long time to be completed (~1 day). Even larger areas could be investigated by collection of multiple images from adjacent areas and the subsequent image stitching. Naturally, the time for acquisition of such 'stitched images' would be even longer.

5. Conclusions

In this communication, we show that the novel AFM-based imaging modality (peak force tapping AFM with quantitative nanomechanical analysis) provides a tool for assessment of nanomechanical properties of multiphase materials that is superior to the currently rather popular statistical nanoindentation technique. We demonstrate that the technique readily provides images (maps) of elastic modulus of heterogeneous microstructures, such as those of the hardened cement pastes, with the lateral resolution comparable to low-keV electron microscopy. From the point of view of the range of the elastic modulus, the technique can distinguish the elastic modulus of about two orders of magnitude difference on the same sample, thus making it suitable for assessment of properties of cement pastes. In particular when correlated with the analysis of datasets based on other analytical techniques, such as those based on the scanning electron microscopy and energy dispersive X-ray spectroscopy, the peak-force tapping AFM shows potential for identification of nanomechanical properties of individual phases of cement pastes. Above that, the paper also demonstrates the importance of the low surface roughness for the assessment of nanomechanical properties.

Acknowledgments

We would like to acknowledge Messrs Luigi Brunetti and Boris Ingold (both EMPA) for the assistance with the sample preparation. We gladly acknowledge that the FIB sample preparation was performed at EMPA, Electronics/Metrology/Reliability Laboratory and Electron Microscopy Centre of ETH Zurich. We thank Mr Daniel Schreier (EMPA) for assistance with EDX analysis. We thank Dr Pietro Lura and Dr Beat Münch (both EMPA) for the critical reading of the manuscript.

References

[1] P. Trtik, J. Dual, B. Münch, L. Holzer, Limitation in obtainable surface roughness of hardened cement paste: 'virtual' topographic experiment based on focussed ion beam nanotomography datasets, J. Microsc.-Oxf. 232 (2008) 200.
[2] P. Trtik, B. Münch, P. Lura, A critical examination of statistical nanoindentation on model materials and hardened cement pastes based on virtual experiments, Cem. Concr. Compos. 31 (2009) 705.
[3] D. Davydov, M. Jirásek, L. Kopecký, Critical aspects of nano-indentation technique in application to hardened cement paste, Cem. Concr. Res. 41 (2011) 20.
[4] P. Lura, P. Trtik, B. Münch, Validity of recent approaches for statistical nanoindentation of cement pastes, Cem. Concr. Compos. 33 (2011) 457.
[5] P. Trtik, P.J.M. Bartos, Micromechanical properties of cementitious composites, Mater. Struct. 32 (1999) 388.
[6] F.-J. Ulm, M. Vandamme, H.M. Jennings, J. Vanzo, M. Bentivegna, K.J. Krakowiak, G. Constantinides, C.P. Bobko, K.J. Van Vliet, Does microstructure matter for statistical nanoindentation techniques? Cem. Concr. Compos. 32 (2010) 92.
[7] C.A. Jones, Z.C. Grasley, Short-term creep of cement paste during nanoindentation, Cem. Concr. Compos. 33 (2011) 12.
[8] W. Zhu, M.T.J. Fonteyn, J. Hughes, C. Pearce, Nanoindentation study of resin impregnated sandstone and early-age cement paste specimens, in: Z. Bittnar, P.J.M. Bartos, J. Nemecek, V. Smilauer, J. Zeman (Eds.), Nanotechnology in Construction 3, Proceedings, Springer-Verlag Berlin, Berlin, 2009, p. 403.
[9] J. Nemecek, V. Smilauer, L. Kopecky, Characterization of alkali-activated fly-ash by nanoindentation, in: Z. Bittnar, P.J.M. Bartos, J. Nemecek, V. Smilauer, J. Zeman (Eds.), Nanotechnology in Construction 3, Proceedings, Springer-Verlag Berlin, Berlin, 2009, p. 337.
[10] P. Schön, K. Bagdi, K. Molnar, P. Markus, B. Pukanszky, G. Julius Vancso, Quantitative mapping of elastic moduli at the nanoscale in phase separated polyurethanes by AFM, Eur. Polym. J. 47 (2011) 692.
[11] W.C. Oliver, G.M. Pharr, An improved technique for determining hardness and elastic-modulus using load and displacement sensing indentation experiments, J. Mater. Res. 7 (1992) 1564.
[12] P. Mondal, S.P. Shah, L. Marks, A reliable technique to determine the local mechanical properties at the nanoscale for cementitious materials, Cem. Concr. Res. 37 (2007) 1440.
[13] M. Heuberger, G. Dietler, L. Schlapbach, Mapping the local Young's modulus by analysis of the elastic deformations occurring in atomic-force microscopy, Nanotechnology 6 (1995) 12.
[14] O. Sahin, N. Erina, High-resolution and large dynamic range nanomechanical mapping in tapping-mode atomic force microscopy, Nanotechnology 19 (2008) 445717.
[15] B. Pittenger, N. Erina, C. Su, Quantitative Mechanical Property Mapping at the Nanoscale with PeakForce QNM, Bruker Corporation Application Note AN128, www.bruker-nano.com2010.
[16] B.V. Derjaguin, V.M. Muller, Y.P. Toporov, Effect of contact deformations on adhesion of particles, J. Colloid Interface Sci. 53 (1975) 314.
[17] J.J. Hughes, P. Trtik, Micro-mechanical properties of cement paste measured by depth-sensing nanoindentation: a preliminary correlation of physical properties with phase type, Mater. Charact. 53 (2004) 223.
[18] J.J. Chen, L. Sorelli, M. Vandamme, F.J. Ulm, G. Chanvillard, A coupled nanoindentation/SEM–EDS study on low water/cement ratio Portland cement paste: evidence for C–S–H/Ca(OH)(2) nanocomposites, J. Am. Ceram. Soc. 93 (2010) 1484.
[19] Avizo® visualisation software, 2D affine registration subroutine.
[20] K.L. Scrivener, Backscattered electron imaging of cementitious microstructures: understanding and quantification, Cem. Concr. Compos. 26 (2004) 935.
[21] P. Trtik, B. Münch, P. Gasser, A. Leemann, R. Loser, R. Wepf, P. Lura, Focussed ion beam nanotomography reveals the 3D morphology of different solid phases in hardened cement pastes, J. Microsc. 241 (2011) 234.
[22] L. Sorelli, G. Constantinides, F.J. Ulm, F. Toutlemonde, The nano-mechanical signature of ultra high performance concrete by statistical nanoindentation techniques, Cem. Concr. Res. 38 (2008) 1447.
[23] K. Velez, S. Maximilien, D. Damidot, G. Fantozzi, F. Sorrentino, Determination by nanoindentation of elastic modulus and hardness of pure constituents of Portland cement clinker, Cem. Concr. Res. 31 (2001) 555.
[24] J.S. Schweitzer, R.A. Livingston, C. Rolfs, H.W. Becker, S. Kubsky, Ion beam analysis of the hydration of tricalcium silicate, Nucl. Instrum. Methods Phys. Res. Sect. B-Beam Interact. Mater. Atoms 207 (2003) 80.
[25] C. Meade, R. Jeanloz, Static compression of $Ca(OH)_2$ at room-temperature — observations of amorphization and equation of state measurements to 10.7 GPa, Geophys. Res. Lett. 17 (1990) 1157.
[26] J.L. Laugesen, Density functional calculations of elastic properties of portlandite, Ca(OH)(2), Cem. Concr. Res. 35 (2005) 199.